

RESEARCH LETTER

10.1029/2018GL077324

Special Section:

New Understanding of the Solar Eclipse Effects on Geospace: The 21 August 2017 Solar Eclipse

Key Points:

- Large-scale citizen science experiment probes eclipse-induced ionospheric changes
- Eclipse effects are observed ± 0.3 hr on 1.8 MHz, ± 0.75 hr on 3.5 and 7 MHz, and ± 1 hr on 14 MHz
- Observations are consistent with an eclipse-induced weakening of the D, E, and F ionospheric regions

Supporting Information:

- Data Set S1
- Text S1
- Text S2

Correspondence to:

N. A. Frissell,
nathaniel.a.frissell@njit.edu

Citation:

Frissell, N. A., Katz, J. D., Gunning, S. W., Vega, J. S., Gerrard, A. J., Earle, G. D., et al. (2018). Modeling amateur radio soundings of the ionospheric response to the 2017 great American eclipse. *Geophysical Research Letters*, 45, 4665–4674. <https://doi.org/10.1029/2018GL077324>

Received 30 JAN 2018

Accepted 6 MAY 2018















Accepted article online 11 MAY 2018

Published online 29 MAY 2018

©2018. The Authors.

This is an open access article under the terms of the Creative Commons Attribution-NonCommercial-NoDerivs License, which permits use and distribution in any medium, provided the original work is properly cited, the use is non-commercial and no modifications or adaptations are made.

Modeling Amateur Radio Soundings of the Ionospheric Response to the 2017 Great American Eclipse

N. A. Frissell¹ , J. D. Katz¹ , S. W. Gunning¹ , J. S. Vega¹ , A. J. Gerrard¹ , G. D. Earle² , M. L. Moses² , M. L. West³ , J. D. Huba⁴ , P. J. Erickson⁵ , E. S. Miller⁶ , R. B. Gerzoff⁷ , W. Liles⁸ , and H. W. Silver⁹ 

¹Center for Solar-Terrestrial Research, New Jersey Institute of Technology, Newark, NJ, USA, ²Virginia Tech, Blacksburg, VA, USA, ³Department of Mathematical Sciences, Montclair State University, Montclair, NJ, USA, ⁴Plasma Physics Division, Naval Research Laboratory, Washington, DC, USA, ⁵Haystack Observatory, Massachusetts Institute of Technology, Westford, MA, USA, ⁶Johns Hopkins University Applied Physics Laboratory, Laurel, MD, USA, ⁷Applied Statistical Consulting, Atlanta, GA, USA, ⁸Independent Consultant, Reston, VA, USA, ⁹American Radio Relay League, Newington, CT, USA

Abstract On 21 August 2017, a total solar eclipse traversed the continental United States and caused large-scale changes in ionospheric densities. These were detected as changes in medium- and high-frequency radio propagation by the Solar Eclipse QSO Party citizen science experiment organized by the Ham Radio Science Citizen Investigation (hamsci.org). This is the first eclipse-ionospheric study to make use of measurements from a citizen-operated, global-scale HF propagation network and develop tools for comparison to a physics-based model ionosphere. Eclipse effects were observed ± 0.3 hr on 1.8 MHz, ± 0.75 hr on 3.5 and 7 MHz, and ± 1 hr on 14 MHz and are consistent with eclipse-induced ionospheric densities. Observations were simulated using the PHaRLAP raytracing toolkit in conjunction with the eclipsed SAMI3 ionospheric model. Model results suggest 1.8, 3.5, and 7 MHz refracted at $h \geq 125$ km altitude with elevation angles $\theta \geq 22^\circ$, while 14 MHz signals refracted at $h < 125$ km with elevation angles $\theta < 10^\circ$.

Plain Language Summary On 21 August 2017, the shadow of the moon traveled across the continental United States from Oregon to South Carolina during a total solar eclipse. While total eclipses are best known for their stunning visual display, they also cause changes to the ionosphere, an electrically charged layer of the upper atmosphere. These changes modify how medium- and high-frequency radio waves (300 kHz to 30 MHz) travel. To help study these changes, ham radio operators communicated with each other before, during, and after the eclipse while automated monitoring systems logged their communications. These logs are compared with outputs of an eclipsed version of the ionospheric research model SAMI3. By comparing observations with the model, we can better understand how the eclipse affected both the ionosphere and radio propagation.

1. Introduction

On 21 August 2017, a total solar eclipse traversed the continental United States (CONUS) from Oregon to South Carolina in just over 90 min. While total eclipses are known for their spectacular visual displays, they also play significant roles in the study of the ionosphere and radio science. Eclipses create predictable yet unusual solar inputs to the upper atmosphere by temporarily blocking ultraviolet (UV) radiation, causing reductions in photoionization and increases in recombination. Detailed work on eclipse ionospheric effects extends back to Benyon and Brown (1956) and Anastassiades (1970), and more recently Evans (1965), Roble et al. (1986), and Krankowski et al. (2008).

Eclipse-induced depletions of ionospheric densities are known to affect propagation on medium- and high-frequency bands (MF and HF, 300 kHz to 30 MHz). This is of great interest to amateur (ham) radio operators, hobbyists licensed by their national governments to transmit on specified frequencies for personal enjoyment. Hams often use MF and HF ionospheric refractions for long-distance communications and enjoy studying space weather and its effects on these communications. Kennedy and Schauble (1970) and Kennedy et al. (1972) conducted solar eclipse D-region absorption experiments using amateur radio,

Bamford (2000) and Bamford (2001) coordinated citizen science experiments during the 1999 total solar eclipse in the United Kingdom, and the Radio Society of Great Britain held a special operating event to study the effects of the 2015 UK partial eclipse (Nichols, 2015).

We build on these previous works with results from the HamSCI Solar Eclipse QSO Party (SEQP), a large-scale citizen science experiment organized by the Ham Radio Science Citizen Investigation (hamsci.org). Hams followed prescribed rules to make as many QSOs (radio contacts) as possible in the area around the eclipse path. Thanks to the participation of over 5,000 hams and the extensive Reverse Beacon Network (RBN; <http://reversebeacon.net>), PSKReporter (Phase Shift Keying Reporter; <http://pskreporter.info>), and WSPRNet (Weak Signal Propagation Reporting Network; <http://wsprnet.org>) automated amateur observing networks, the HamSCI SEQP has generated a comprehensive total solar eclipse MF and HF propagation data set with greater spatial, temporal, and spectral coverage than any prior amateur radio citizen science experiment. Here we present SEQP observations collected on a continental scale to show eclipse-induced ionospheric effects.

A large-scale simulation of the SEQP was calculated by raytracing links between a grid of theoretical transmitters and selected receiver locations using the PHaRLAP raytracing toolkit (Cervera & Harris, 2014) with an eclipsed version of the Naval Research Laboratory SAMI3 ionospheric model (Huba & Drob, 2017). Results are consistent with a decrease in D-layer absorption and a weakening of the F layer. By comparing data with model results, we constrain the likely refraction altitudes of the amateur radio observations, test the validity of model propagation paths, and demonstrate a technique that relates amateur radio spot data to research-grade ionospheric models.

2. Data and Methodology

2.1. Amateur Radio Observations

Amateur radio operators voluntarily operate a number of fully automated communication observation networks. These systems include PSKReporter, WSPRNet, and the RBN. These networks can monitor and log digital and Morse code signals across the amateur radio bands, especially those between 1.8 and 50 MHz. Each datum ("spot") includes the call signs of both the transmitting and receiving stations, as well as the time, frequency, and mode of communication. Locations of the stations are either provided with the datum or may be determined via a database look-up. Frissell et al. (2014) demonstrated that observations from these systems can be used to study ionospheric effects, such as HF radio absorption due to a solar flare.

2.1.1. Solar Eclipse QSO Party

Figure 1a shows a map of RBN observations, transmitters, and receivers from 1400–2200 UT on 21 August 2017, from 2 hr before first contact of partial eclipse in Oregon to 2 hr after final contact in South Carolina. These include measurements from the 1.8 MHz (160 m), 3.5 MHz (80 m), 7 MHz (40 m), 14 MHz (20 m), 21 MHz (15 m), 28 MHz (10 m), and 50 MHz (6 m) amateur radio bands. Spot color represents the maximum fraction of solar disk obscuration at 300 km altitude O_{300} at that location, as calculated with Frissell (2017). This altitude was selected as reasonable for ionospheric refraction. The location, large-scale geographic distribution, and high number density of spots in Figure 1a shows that the RBN has excellent coverage of the CONUS. The path of totality appears clearly as a dark red band extending from the northwest to the southeast United States.

The dense coverage of RBN spots shown in Figure 1a can be attributed to the SEQP, a special event organized by HamSCI specifically for studying this eclipse. "QSO" is amateur radio parlance for a two-way contact, and a "QSO Party" is typically a contest-like event in which predefined rules govern the behavior of the participants. Bonus and multiplier points are awarded to incentivize desired behaviors. In the case of this SEQP, participants were encouraged to make as many contacts with as many geographic locations as possible on specified amateur radio bands. Contacts made with modes that could be automatically detected by the RBN and PSKReporter were worth twice as many points as those that could not. The final official version of the SEQP rules are provided as a PDF in the supporting information and is described in more detail by Frissell et al. (2017).

Data from the SEQP were obtained from manual logs submitted by participants to hamsci.org, as well as observations made by the RBN, PSKReporter, and WSPRNet. Geolocation data were determined first from participant-submitted logs, then spot data, and finally qrz.com database look-ups. In total over 30,700 log, 618,000 RBN, 630,000 WSPRNet, and 1,287,000 PSKReporter spots were reported for the duration of the SEQP. These large numbers were made possible thanks to SEQP publicity provided by the American Radio

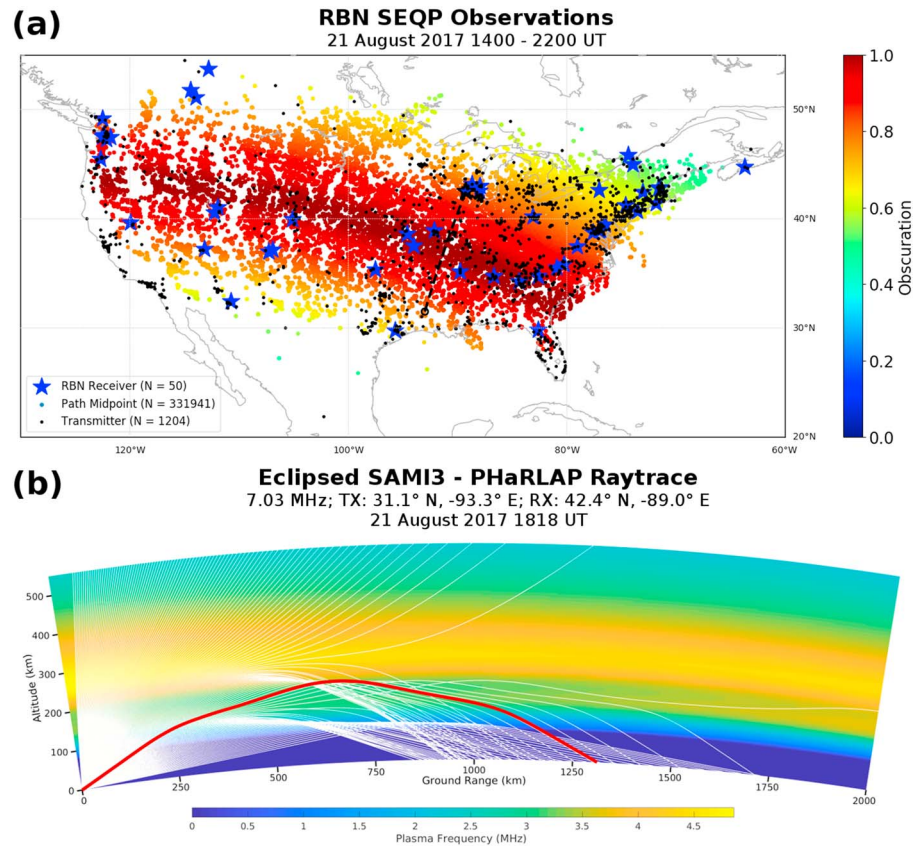


Figure 1. (a) RBN observations during the All-American total solar eclipse on 21 August 2017. Midpoints between transmitter and RBN receiver are color coded by their maximum obscuration. RBN receivers are marked as blue stars, and transmitters are represented by black dots. Note the dark path of totality from Oregon to South Carolina. (b) Two-dimensional PHaRLAP raytrace of 7.03 MHz through the eclipsed SAMI3 ionosphere. The black dashed line in (a) shows the path between the transmitter and receiver. RBN = Reverse Beacon Network; SEQP = Solar Eclipse QSO Party.

Relay League (ARRL; arrl.org), the U.S. national association for amateur radio (e.g., Silver, 2017) and the active involvement of each amateur voluntarily operating in the SEQP or running a data collection facility.

This paper uses spot data only from the RBN. Data publicly available from the RBN website undergo a certain level of filtering to prevent stations from being spotted more than once every 10 min. An unfiltered data archive provided by the RBN operators was used for our analysis. To focus on eclipse effects, we required both the transmitter and RBN receiver to be in the region bounded by $20^\circ \leq \text{lat} < 55^\circ$ and $-130^\circ \leq \text{lon} < -60^\circ$, as shown in the Figure 1a map. Furthermore, we only used data with great circle paths $R_{gc} < 3,000$ km, which should select primarily for single-hop communications. Assuming specular reflection, a 0° takeoff angle, and Earth radius $R_e = 6,371$ km, the theoretical limit for single-hop F-layer (300 km alt) propagation is $R_{gc} = 3,835$ km and single-hop E-layer (110 km alt) propagation is $R_{gc} = 2,351$ km.

2.2. PHaRLAP-Eclipsed SAMI3

We compared the RBN SEQP observations to a theoretical simulation by raytracing radio signals through a numerical prediction of the eclipsed ionosphere. This simulation predicts whether or not a communication link between two points at a specified time and frequency is possible, as well as the likely path of the ray. For the ionosphere, we used a prediction generated by the SAMI3 first-principles model using a solar extreme UV radiation mask with a maximum obscuration of 0.85 applied to model inputs (Huba et al., 2000; Huba & Drob, 2017). Although the eclipse is total for visible light, it is not at extreme UV wavelengths that are responsible for F region ionization. Additional SAMI3 input parameters were $F_{10.7} = 90$, $F_{10.7A} = 90$, $Ap = 4$, and day of year 233. The SAMI3 electron density was interpolated to a grid $[n_\phi, n_\theta, n_h] = (100, 360, 100)$ used in this analysis. Here the latitude range is $-90^\circ < \phi < 90^\circ$, longitude range is $-180^\circ < \theta < 180^\circ$, and altitude range is $93 < h < 600$ km. The SAMI3 model does not have a D region ionosphere.

Raytracing through the SAMI3 ionosphere is computed using the PHaRLAP raytracing toolkit (Cervera & Harris, 2014) 2-D engine, which is based on the raytracing scheme developed by Coleman (1997, 1998). Figure 1b presents an example of raytracing from a transmitter located at 31.1° N, -93.3° E ($R_{gc} = 0$ km) to a receiver at 42.4° N, -89.0° E ($R_{gc} = 1,313$ km) at 1818 UT, the time of maximum eclipse at the midpoint of this path. This path is marked as a dashed line on the map in Figure 1a. The 2-D ionosphere is obtained by interpolating through the 3-D SAMI3 grid along the path from the transmitter to the receiver with range extending to 4,000 km in 20 km steps and altitude to 600 km in 3 km steps. A fan of rays with elevation angles from 3° to 85° with 0.5° steps are launched from the transmitter. Propagation is restricted to single hop. An iterative process is used to determine which ray, if any, reaches the receiver. The successful ray is indicated in red on Figure 1b. Behavior of the rays is highly dependent on elevation angle. In general, low elevation angles refract off the E region, midrange elevation angle rays refract off the F region, and elevation angles above the critical angle escape into space.

In the simulation presented in section 3.3, we raytraced 1.83, 3.53, 7.03, and 14.03 MHz between each transmitter in a theoretical grid to every RBN receiver observed during the SEQP at a 3-min cadence from 1600 to 2357 UT. The transmitter grid is an offset grid spaced every 2° longitude and 1° latitude in the CONUS, represented as black dots in the maps of Figures 3a and 4a. All other simulation parameters are as described above.

3. Observations and Model Results

3.1. Geomagnetic Conditions

This eclipse took place toward the bottom of the declining phase of Solar Cycle 24. F10.7 radio flux was 88. Geomagnetic and solar conditions were quiet during the SEQP, thereby increasing the probability that departures from expected propagation were due to eclipse effects and not geomagnetic activity. For the period of 21 August 2017 1400–2200 UT, K_p remained less than 3, and the disturbance storm time index ranged $-19 < DST < -12$ nT. The National Oceanic and Atmospheric Administration Geostationary Operational Environmental Satellite spacecraft detected two minor flares (<C3 class) at 1800 and 2030 UT. There were only six small sunspots visible.

3.2. Ham Radio Observations

Figure 2 presents a map and time series of RBN observations around the time of the eclipse. RBN midpoints at locations with maximum obscuration $O_{300} \geq 0.9$ and frequencies in the 1.8, 3.5, and 14 MHz amateur radio bands have been selected. Bands above 14 MHz are omitted because very few spots were observed at these frequencies. Time is restricted to ± 1.5 hr from eclipse maximum at the location of each midpoint. The map of Figure 2a includes transmitters, RBN receivers, and midpoints color coded by maximum obscuration. Figures 2b–2e are spot midpoint density contours of transmitter-receiver great circle path length R_{gc} versus epoch time relative to maximum eclipse at the location of each midpoint. The underlying grid is 500 km by 10-min bins. For reference, the O_{300} eclipse obscuration curve for 40° N, 100° W (roughly in the center of the CONUS) is overplotted as a white dashed line. Maximum eclipse of $O_{300} = 0.97$ for this location occurred at 1800 UT, 1120 solar local time, 30° solar zenith angle.

Each ham radio band responded differently during the eclipse. Near epoch hour 0, there is a wide gap at 14 MHz, a rise in range at 7 MHz and a strengthening plus a rise in range at both 1.8 and 3.5 MHz. On 14 MHz, Figure 2b shows strong activity before the eclipse from epoch $-1.5 \lesssim t \lesssim -0.5$ hr and ranges $1,000 \lesssim R_{gc} \lesssim 2,000$ km. During the eclipse, the peak number of spots decreases three folds during the period $-0.5 \lesssim t \lesssim 0.5$ hr. After the eclipse, starting at $t \approx 0.5$ hr, activity slowly returns to moderate levels but never quite makes a full recovery.

The 7 MHz band exhibits somewhat opposite behavior from that of the 14 MHz band during the eclipse. Figure 2c again shows strong activity prior to eclipse maximum, but lower in range, centered around $R_{gc} \approx 500$ km from epoch $-1.5 \lesssim t \lesssim -0.25$ hr. As the moon's shadow sweeps across the midpoints in the half hour after epoch hour -1 , the spot density doubles and also widens in range from 300 km wide ($400 \lesssim R_{gc} \lesssim 700$ km) up to 1,200 km wide ($100 \lesssim R_{gc} \lesssim 1,300$ km). Then, at epoch $t \approx -0.25$ hr the spot density band narrows but remains strong as it begins to move outward in range from 500 to 1,000 km with a width of 900 km ($600 \lesssim R_{gc} \lesssim 1,500$ km). After totality the spot density band moves back inwards to a range of 500 km, while the spot density decreases three folds from 300 at $t \approx 0.5$ hr to 100 at $t \approx 1.5$ hr. Activity remains strong at first and then tapers to moderate then quiet levels starting at $t \approx 0.75$ hr.

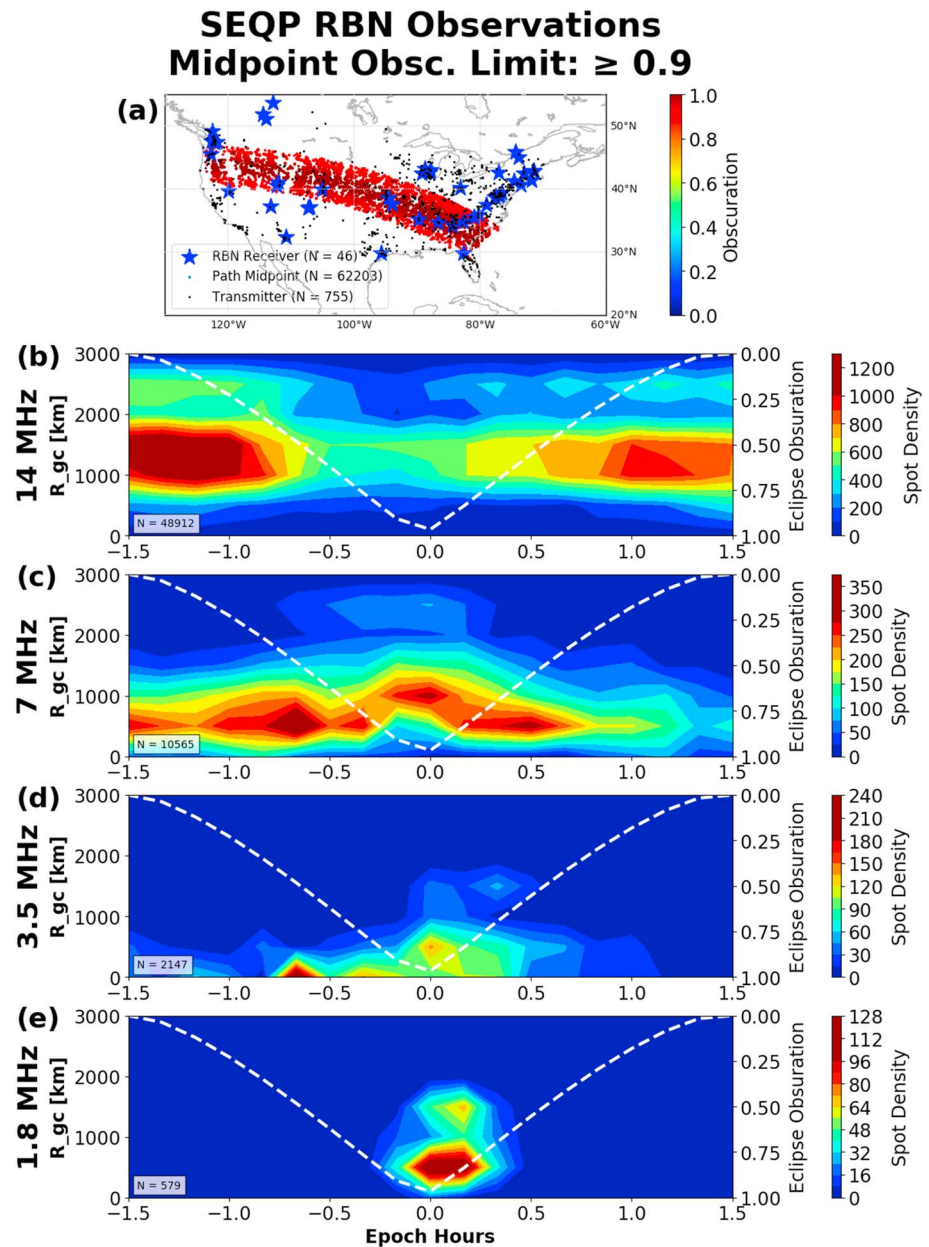


Figure 2. RBN spot observations near the time of totality (maximum obscuration $O_{300} \geq 0.9$). Location of midpoints on map of continental United States (a). Great circle distance between transmitter and receiver versus epoch time for frequencies in the amateur radio bands (b) 14 MHz, (c) 7 MHz, (d) 3.5 MHz, and (e) 1.8 MHz color coded by spot density. For the contours, the underlying grid is 500 km by 10-min bins. The dashed white line shows obscuration at a representative point 40° N, 100° W. RBN = Reverse Beacon Network; SEQP = Solar Eclipse QSO Party.

The 3.5 MHz (Figure 2d) and 1.8 MHz (Figure 2e) ham radio bands exhibit similar behavior to each other. On both bands, there are zero to few spots for substantial portions of time before and after eclipse maximum. Figure 2d shows little activity was observed until epoch $t \lesssim -0.75$ hr when $O_{300} \approx 0.35$. At this point, 3.5 MHz begins to show moderate activity at $R_{gc} \lesssim 500$ km and later $R_{gc} \lesssim 1,000$ km starting at $t \approx 0$ hr. The band returns to pre-eclipse conditions of little to no activity at $t \approx 0.5$ hr when $O_{300} \approx 0.55$. The 1.8 MHz band shows similar behavior; however, the band opening is shorter and more focused around the time of eclipse maximum. No activity is observed from epoch $-1.5 \lesssim t \lesssim 0.25$ hr. At $t \approx 0.25$ hr, a relatively strong band of activity appears at $R_{gc} \approx 500$ km, while a moderate band of activity appears at $R_{gc} \approx 1,500$ km. All observed activity ceases by $t \approx 0.5$ hr, marking a return to pre-eclipse conditions.

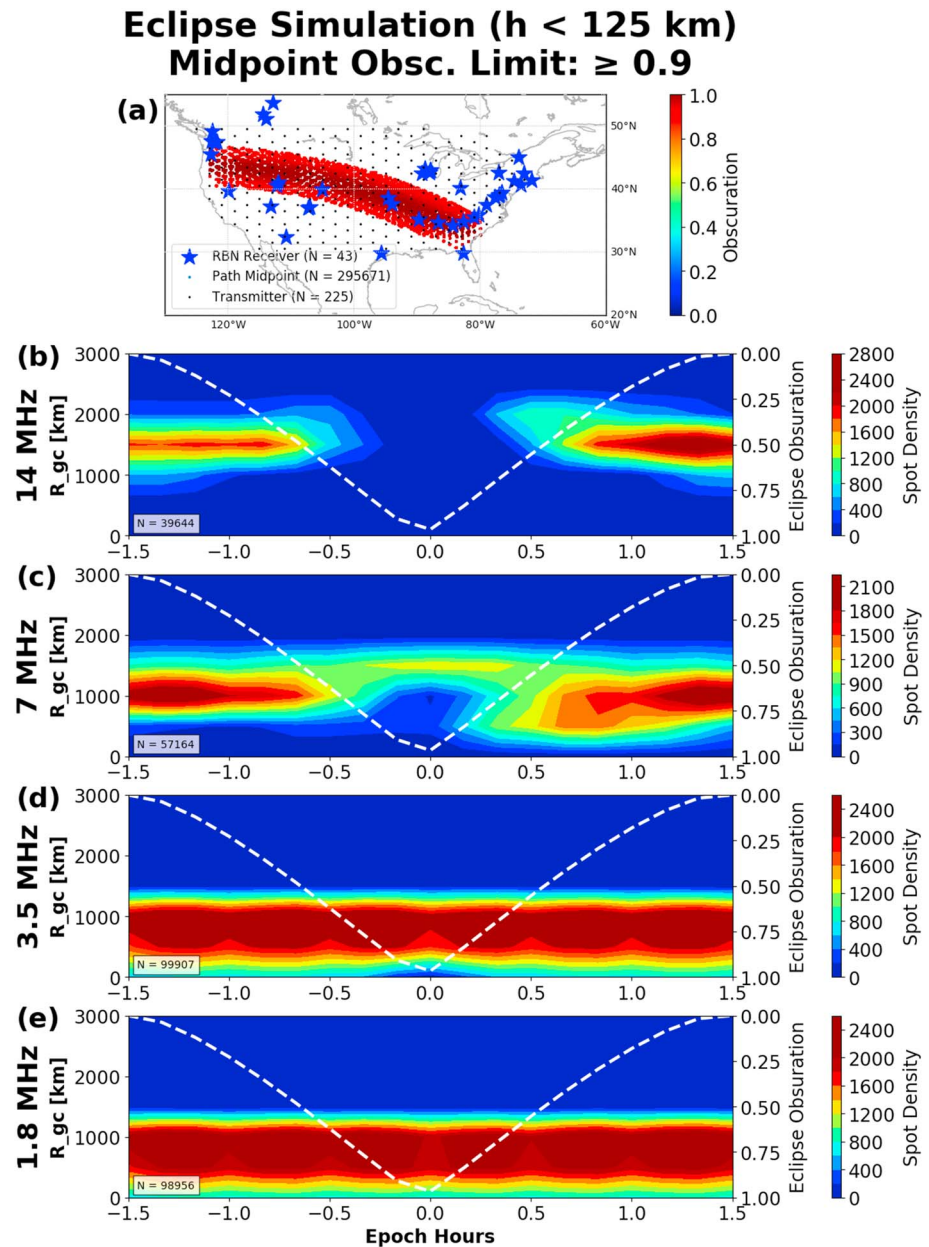


Figure 3. PHaRLAP-SAMI3 simulations for reflections from altitudes < 125 km. Descriptions as in Figure 2. RBN = Reverse Beacon Network.

3.3. Raytracing Results

To aid in RBN observation interpretation, we ran a simulation of the SEQP by raytracing links between a grid of theoretical transmitters and subset of RBN receivers using the PHaRLAP raytracing toolkit in conjunction with an eclipsed version of the SAMI3 ionospheric model. Details of this methodology have been provided in section 2.2. The results of this model run were visualized in the same format as Figure 2 to allow for direct comparison to RBN data.

Plots of the initial visualization were saturated and obscured eclipse effects. It was found that good data-model agreement could be achieved by separating the model results by refraction apogee (altitude), and that all RBN bands did not appear to refract from the same altitude. Section 3.3.1 presents raytracing results for refraction altitudes $h < 125$ km, while section 3.3.2 presents raytracing results for refraction altitudes $h \geq 125$ km.

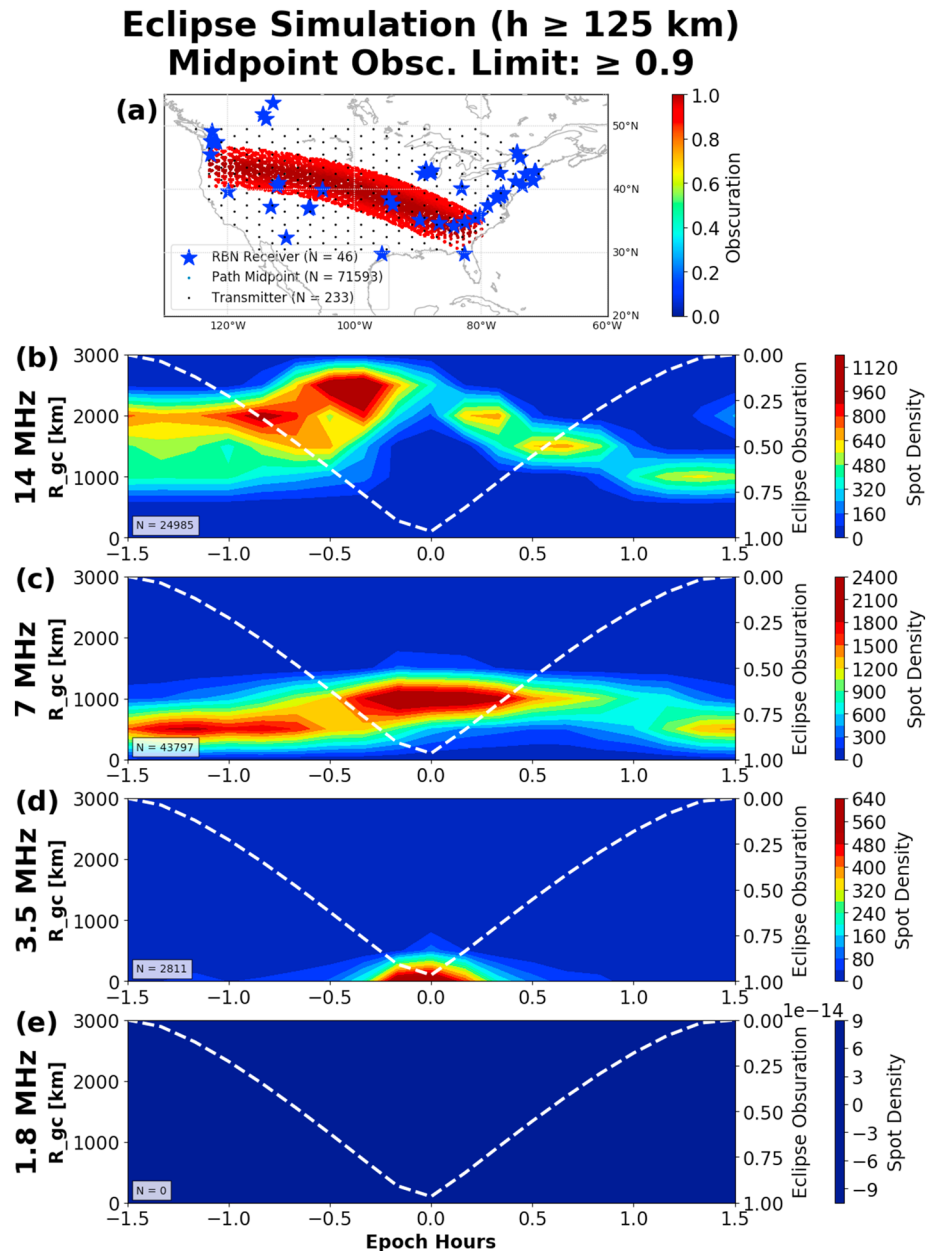


Figure 4. PHaRLAP-SAM3 simulations for reflections from altitudes ≥ 125 km. Descriptions as in Figure 2. RBN = Reverse Beacon Network.

3.3.1. Raytrace Refractions < 125 km Altitude

Figure 3 presents raytracing results for refraction altitudes $h < 125$ km altitude in the same format as the RBN observations in Figure 2. Figure 3a shows the locations of simulated transmitters, receivers, and the midpoints. The black transmitter dots are now configured in a checkerboard-grid configuration rather than the quasi-random placement of real transmitters shown in Figure 2a.

On 14 MHz, there is a band of strong activity that occurs from $-1.5 \lesssim t \lesssim -0.5$ hr centered at $R_{gc} \approx 1,500$ km and spread between $1,200 \lesssim R_{gc} \lesssim 1,800$ km. The number of successful raytrace links drops to 0 between $-0.5 \lesssim t \lesssim 0.5$ hr when $O_{300} \lesssim 0.60$. Full recovery occurs shortly after $t \approx 0.5$, as strong activity appears again $1,200 \lesssim R_{gc} \lesssim 1,800$ km. Model output indicates the mean elevation angle is $\theta < 10^\circ$ for all spot bins in this figure. Comparison of the simulated spots of Figure 3b with the 14 MHz RBN observations of Figure 2b shows generally good agreement in range and spot density before, during, and after eclipse maximum.

The 7 MHz simulation for $h < 125$ km is shown in Figure 3c. In the period before eclipse maximum from $-1.5 \lesssim t \lesssim -0.5$ hr, a band of strong activity is centered at $R_{gc} \approx 1,000$ km. From $-0.5 \lesssim t \lesssim 0.5$ hr, the activity band narrows and moves out in range to $R_{gc} \approx 1,500$ km. Post-eclipse recovery begins at $t \approx 0.5$ hr when the activity band moves back to $R_{gc} \approx 1,000$ km. Before and after the eclipse effect when $R_{gc} \approx 1,000$ km, all mean elevation angles are $\theta \lesssim 27^\circ$. During the main eclipse effect when $R_{gc} \approx 1,500$ km, all mean elevation angles reduce to $\theta \lesssim 15^\circ$. When the 7 MHz model results of Figure 3c are compared to Figure 2c observations, it can be seen that model ranges are approximately 500 km greater than RBN ranges at all times.

In Figure 3d, the 3.5 MHz $h < 125$ km simulation results show that propagation is nearly unchanged for the entire period, with large amounts of activity predicted for ranges $R_{gc} \lesssim 1,250$ km. Model transmit elevation angle is $\theta < 60^\circ$ for all spots. A very small eclipse effect can be seen from $-0.25 \lesssim t \lesssim 0.25$ hr, when a small bite-out in predicted activity is observed at $R_{gc} \lesssim 250$ km. At this time, elevation angles reduce to $\theta < 36^\circ$. The 3.5 MHz simulation results are practically opposite of the 3.5 MHz RBN observations presented in Figure 2d. The 1.8 MHz $h < 125$ km simulation of Figure 3e is nearly identical to the 3.5 MHz $h < 125$ km results, except the eclipse effect is almost nonexistent. Similar to the 3.5 MHz $h < 125$ km results, the 1.8 MHz $h < 125$ km simulation is in strong disagreement with the RBN observations in Figure 2e.

3.3.2. Raytrace Refractions ≥ 125 km Altitude

Figure 4 presents raytracing results for refraction altitudes $h \geq 125$ km altitude. The figure format is the same as Figures 2 and 3. Figure 4a shows the locations of simulated transmitters, receivers, and midpoints. Figure 4b presents the 14 MHz $h \geq 125$ km simulation results. From $-1.5 \lesssim t \lesssim -0.5$ hr, a moderately active band exists between $1,000 \lesssim R_{gc} \lesssim 2,200$ km with elevation angles between $10^\circ < \theta < 20^\circ$. Just before maximum obscuration, from $-0.5 \lesssim t \lesssim 0$ hr, the activity moves outward and a hotspot forms at $R_{gc} \approx 2,500$ km. Starting at $t \approx 0$ hr, activity weakens and gradually moves inward until it stabilizes at $t \approx 1$ hr and $R_{gc} \approx 1,000$ km. After $t \approx 0$ hr, elevation angles reduce to $\theta < 15^\circ$. The $h \geq 125$ km simulation results are farther in range and predict significantly more activity in the period $-0.5 \lesssim t \lesssim 0$ hr than the RBN observations of Figure 2b. Therefore, these model results do not show good agreement with 14 MHz observations.

Figure 4c shows the 7 MHz $h \geq 125$ km simulation results. An active band is predicted from $-1.5 \lesssim t \lesssim -0.5$ hr in a band around $R_{gc} \approx 500$ km. From $-0.5 \lesssim t \lesssim 0.5$ hr, the activity band intensifies and moves out in range to $R_{gc} \approx 1,000$ km. Starting at $t \approx 0.5$ hr, the predicted activity decreases and the range moves back to $R_{gc} \approx 1,000$ km. Before and after the eclipse effect when $R_{gc} \approx 500$ km, elevation angles range from $35^\circ \lesssim \theta \lesssim 47^\circ$. When $R_{gc} \approx 1,000$ km near maximum obscuration, elevation angles range from $22^\circ \lesssim \theta \lesssim 35^\circ$. These simulation results for 7 MHz $h \geq 125$ km show good agreement in range and morphology with the 7 MHz RBN observations of Figure 2c.

Results for the 3.5 MHz $h \geq 125$ km simulation are presented in Figure 4d. No activity is predicted except at $R_{gc} \lesssim 250$ km an hour around eclipse maximum ($-0.5 \lesssim t \lesssim 0.5$ hr). Elevation angles are high, ranging between $47^\circ < \theta < 83^\circ$. This simulation is somewhat consistent with the 3.5 MHz RBN observations of Figure 2d. The 1.8 MHz $h \geq 125$ km simulation of Figure 4e shows no predicted spots, even though activity was observed around eclipse maximum in the Figure 2e RBN data.

4. Discussion

The PHaRLAP-SAMI3 simulation produced results that are a combination of Figures 3 and 4. Separating results by refraction altitude of $h = 125$ km allows the comparison of simulation results (Figures 3 and 4) to the RBN observations (Figure 2) and the selection of the most correct model solution for each band. It is then possible to both make constraints on the model and use the model to assist in the interpretation of the RBN ham radio observations. In section 3, it was found that the 14 MHz band is most consistent with refraction altitudes $h < 125$ km, while the 1.8, 3.5, and 7 MHz observations are most consistent with refraction altitudes $h \geq 125$ km.

The results presented here can be explained with a discussion of D region absorption, critical angles, and critical frequencies. From the model, rays that refract at $h < 125$ km generally have lower elevation angles than rays that refract at $h \geq 125$ km. For a specified frequency, ionospheric, and magnetic configuration, lower-angle signals spend more time in the D region and suffer greater absorption. Rays that refract at $h \geq 125$ km have higher elevation angles and are more likely to exceed the critical angle for a layer. If that occurs, the ray will pass on to the next layer or escape into space. Decreased ionization levels, such as those

associated with the eclipse shadow, will decrease the D region absorption, critical angle, and critical frequency along a path. Most ionospheric communications refract off the E or F layers, with lower frequencies experiencing greater refraction for a given ionospheric state.

The agreement of 14 MHz observations with the $h < 125$ km simulation suggests low-angle 14 MHz signals were below the E region cutoff frequency before and after the eclipse. During the eclipse, ionospheric densities dropped such that low-angle paths escaped to space. Poor data-model agreement for $h \geq 125$ km suggests ionospheric densities were never sufficient to support high-angle 14 MHz rays. The 3.5 and 7 MHz observations were found to be most consistent with the $h \geq 125$ km simulation (high-angle rays). The 7 MHz simulation shows decreases in ionospheric densities are associated with R_{gc} lengthening. 3.5 MHz simulation rays are trapped below $h = 125$ km before and after the eclipse but penetrate to higher altitudes as densities decrease.

Although SAMI3-PHaRLAP does not include D region absorption, certain D region effects may be inferred. On low-altitude/low-angle paths, SAMI3-PHaRLAP predicts almost constant 1.8 and 3.5 MHz communications, as well as extended range 7 MHz communications. These signals are not observed by the RBN, likely attributable to D region absorption. At high obscuration, absorption is likely reduced and more 1.8 and 3.5 MHz RBN signals are observed. Data-model comparison also reveals SAMI3-PHaRLAP predicted high-altitude 14 MHz and low-altitude 1.8 and 3.5 MHz rays not observed by the RBN, suggesting that SAMI3 electron densities are too high. An iterative process could potentially be used to determine a scaling factor to be applied to model densities in order to minimize errors with observations.

In general, this paper found results consistent with previous eclipse-ionospheric studies, including citizen science studies such as Bamford (2000) and Kennedy and Schauble (1970). However, this is the first study to make use of measurements from a citizen-operated, global-scale HF propagation network and develop tools for comparison to a physics-based model ionosphere. Data-model comparison has enabled geophysical interpretation of RBN observations by allowing the frequency-dependent identification of refraction altitude and usable elevation angles.

5. Conclusions

On 21 August 2017, a total solar eclipse traversed the CONUS and caused large-scale changes in ionospheric densities. These were detected as changes in medium- and high-frequency radio propagation by the SEQP citizen science experiment organized by the Ham Radio Science Citizen Investigation (hamsci.org). This is the first eclipse-ionospheric study to make use of measurements from a citizen-operated, global-scale HF propagation network and develop tools for comparison to a physics-based model ionosphere. Eclipse effects were observed ± 0.3 hr on 1.8 MHz, ± 0.75 hr on 3.5 and 7 MHz, and ± 1 hr on 14 MHz and are consistent with eclipse-induced ionospheric densities. Observations were simulated using the PHaRLAP raytracing toolkit in conjunction with the eclipsed SAMI3 ionospheric model. Model results suggest 1.8, 3.5, and 7 MHz refracted at $h \geq 125$ km altitude with elevation angles $\theta \geq 22^\circ$, while 14 MHz signals refracted at $h < 125$ km with elevation angles $\theta < 10^\circ$.

References

- Anastassiades, M. (Ed.) (1970). *Solar eclipses and the ionosphere: A NATO Advanced Studies Institute held in Lagonissi, Greece, May 26–June 4, 1969*. New York: Plenum Press.
- Bamford, R. (2000). Radio and the 1999 UK total solar eclipse (D48-1). Chilton, Didcot, UK: Rutherford Appleton Laboratory.
- Bamford, R. (2001). The effect of the 1999 total solar eclipse on the ionosphere. Physics and chemistry of the Earth, part C: Solar. *Terrestrial and Planetary Science*, 26(5), 373–377. [https://doi.org/10.1016/S1464-1917\(01\)00016-2](https://doi.org/10.1016/S1464-1917(01)00016-2)
- Benyon, W. J. G., & Brown, G. M. (Eds.) (1956). *Solar eclipses and the ionosphere, Proceedings of the Symposium Held Under the Auspices of the International Council of Scientific Unions Mixed Commission on the Ionosphere in London, August 1955*. Pergamon Press.
- Cervera, M. A., & Harris, T. J. (2014). Modeling ionospheric disturbance features in quasi-vertically incident ionograms using 3-D magnetoionic ray tracing and atmospheric gravity waves. *Journal of Geophysical Research: Space Physics*, 119, 431–440. <https://doi.org/10.1002/2013JA019247>
- Coleman, C. J. (1997). On the simulation of backscatter ionograms. *Journal of Atmospheric and Solar-Terrestrial Physics*, 59(16), 2089–2099. [https://doi.org/10.1016/S1364-6826\(97\)00038-2](https://doi.org/10.1016/S1364-6826(97)00038-2)
- Coleman, C. J. (1998). A ray tracing formulation and its application to some problems in over-the-horizon radar. *Radio Science*, 33(4), 1187–1197. <https://doi.org/10.1029/98RS01523>
- Evans, J. V. (1965). An F region eclipse. *Journal of Geophysical Research*, 70(1), 131–142. <https://doi.org/10.1029/JZ070i001p00131>
- Frissell, N. A. (2017). Eclipse obscuration calculator, Github/Zenodo. <https://doi.org/10.5281/zenodo.1120440>
- Frissell, N. A., Miller, E. S., Kaepller, S. R., Ceglia, F., Pascoe, D., Sinanis, N., et al. (2014). Ionospheric sounding using real-time amateur radio reporting networks. *Space Weather*, 12, 651–656. <https://doi.org/10.1002/2014SW001132>

Acknowledgments

NAF acknowledges the support of NSF Grant AGS-1552188/479505-19C75. K_p and DST indices were obtained from the Kyoto WDC. F10.7 data were accessed through the OMNI database at the NASA Space Physics Data Facility. GOES data are provided by NOAA SWPC. RBN data are provided by reversebeacon.net, with thanks to F. Ceglia, P. Smith, and R. Williams. We thank the global amateur radio community and the ARRL for making the SEQP possible. The results published in this paper were obtained using the HF propagation toolbox, PHaRLAP, created by Manuel Cervera, Defence Science and Technology Group, Australia (manuel.cervera@dsto.defence.gov.au). This toolbox is available by request from its author. SAMI3 outputs are available by contacting J. Huba at huba@nrl.navy.mil. We acknowledge the use of the Free Open Source Software projects used in this analysis: Ubuntu Linux, python, matplotlib, NumPy, SciPy, pandas, and others. NAF thanks R. M. Frissell and L. J. Lanzerotti for helpful discussions.

- Frissell, N. A., Vega, J. S., Katz, J. D., Gunning, S. W., Gerrard, A. J., Moses, M. L., et al. (2017). HamSCI and the 2017 total solar eclipse. In *ARRL and TAPR Digital Communications Conference* (Vol. 36, pp. 1–21). Newington, CT: Tucson Amateur Packet Radio, American Radio Relay League.
- Huba, J. D., & Drob, D. (2017). SAMI3 prediction of the impact of the 21 August 2017 total solar eclipse on the ionosphere/plasmasphere system. *Geophysical Research Letters*, *44*, 5928–5935. <https://doi.org/10.1002/2017GL073549>
- Huba, J. D., Joyce, G., & Fedder, J. A. (2000). Sami2 is another model of the ionosphere (SAMI2): A new low-latitude ionosphere model. *Journal of Geophysical Research*, *105*(A10), 23,035–23,053. <https://doi.org/10.1029/2000JA000035>
- Kennedy, J. R., & Schauble, J. J. (1970). Preliminary results of a radio absorption study at 3.5 MHz. *Nature*, *226*, 1118–1119. <https://doi.org/10.1038/2261118a0>
- Kennedy, J., Schauble, J., Allnoch, J., & Roberts, D. (1972). D-layer absorption during a solar eclipse. *Quantum Science and Technology*, *7*, 40–41.
- Krankowski, A., Shagimuratov, I. I., Baran, L. W., & Yakimova, G. A. (2008). The effect of total solar eclipse of October 3, 2005, on the total electron content over EuropeKran. *Advances in Space Research*, *41*(4), 628–638. <https://doi.org/10.1016/j.asr.2007.11.002>
- Nichols, S. (2015). Partial eclipse 2015: Solar eclipse propagation experiments yield valuable data. *RadCom*, 22–26.
- Roble, R. G., Emery, B. A., & Ridley, E. C. (1986). Ionospheric and thermospheric response over Millstone Hill to the May 30, 1984, annular solar eclipse. *Journal of Geophysical Research*, *91*(A2), 1661–1670. <https://doi.org/10.1029/JA091iA02p01661>
- Silver, H. W. (2017). The solar eclipse QSO party. *QST*, *101*(2), 82–84.